A multi-domain gem-grade Brazilian apatite

Baikie, Tom; Schreyer, Martin K.; Wong, Chui Ling; Pramana, Stevin S.; Klooster, Wim T.; Ferraris, Cristiano; McIntyre, Garry J.; White, Timothy John

2012

Baikie, T., Schreyer, M. K., Wong, C. L., Pramana, S. S., Klooster, W. T., Ferraris, C., et al. (2012). A multi-domain gem-grade Brazilian apatite. American Mineralogist, 97(10), 1574-1581.

https://hdl.handle.net/10356/98365

https://doi.org/10.2138/am.2012.4069

Revised Manuscript

A Multi-Domain Gem-Grade Brazilian Apatite

Tom Baikie,[1] Martin K. Schreyer,[2] Chui Ling Wong,[1] Stevin S. Pramana,[1] Wim T. Klooster,[3] Cristiano Ferraris,[4] Garry J. McIntyre,[3] and T. J. White[5]

[1] School of Materials Science and Engineering, Nanyang Technological University, Nanyang Avenue, 639798 Singapore.

[2] Institute of Chemical Engineering Sciences, 1 Pesek Road, Jurong Island, Singapore.

[3] The Bragg Institute, Australian Nuclear Science and Technology Organisation, Lucas Heights, NSW 2234, Australia.

[4] Laboratoire de Minéralogie, USM 201, Muséum National d'Histoire Naturelle, CP 52, 61 Rue Buffon, 75005 Paris, France.

[5] Centre of Advanced Microscopy, The Australian National University, Canberra ACT 0200, Australia.

* Corresponding Author: tbaikie@ntu.edu.sg

Abstract

A gem-grade apatite from Brazil of general composition $(Ca,Na)_{10}[(P,Si,S)O_4]_6(F,Cl,OH)_2$ has been studied using single-crystal X-ray and neutron diffraction together with synchrotron powder X-ray diffraction. Earlier electron-microscopy studies had shown the nominally single-phase apatite contains an abundant fluorapatite (F-*Ap*) host, together with chloro-hydroxylapatites (Cl/OH-*Ap*) guest phases that encapsulate hydroxylellestadite (OH-*El*) nanocrystals. While the latter features appear as small (200-400 nm) chemically distinct regions by transmission electron microscopy, and can be identified as separate phases by synchrotron powder X-ray diffraction, these could not be detected by single-crystal X-ray and neutron analysis. The observations using neutron, X-ray and electron probes are however consistent and complementary. After refinement in the space group $P6_3/m$ the tunnel anions F^- are fixed at z = ¼ along <001>, while the anions Cl^- and OH^- are disordered, with the suggestion that O-H···O-H··· hydrogen-bonded chains form in localised regions, such that no net poling results. The major cations are located in the 4*f* A^FO_6 metaprism (Ca + Na), 6*h* A^TO_6X tunnel site (Ca only) and 6*h* BO_4 tetrahedron (P + Si + S). The structural intricacy of this gem stone provides further evidence that apatite microstructures display a nano-phase separation that is generally unrecognized, with the implication that such complexity may impact upon the functionality of technological analogues.

Introduction

Apatite *sensu stricto* has the composition $Ca_{10}(PO_4)_6(F,Cl,OH)_2$, with fluorapatite (F-*Ap*) (Sudarsanan et al., 1972), hydroxylapatite (OH-*Ap*) (Kay et al., 1964) and chlorapatite (Cl-*Ap*) (Mackie et al., 1972) as the designated end members. Natural and synthetic analogues generally conform to hexagonal $P6_3/m$ symmetry and the crystal chemical formula $[A^{F}{}_4][A^{T}{}_6][(BO_4)_6]X_2$ where *A* includes the larger cations, *B* are metalloids, and *X* the halides or oxy-anions (White and Dong, 2003). Lower-symmetry counterparts are realized through atomic ordering within, or topological adjustments of, the putative $A^{F}{}_4(BO_4)_6$ zeolite-like framework that creates $[001]_{hex}$ tunnels surrounding the $A^{T}{}_6X_2$ component (Fig. 1). The diameter of this passage adjusts through anti-symmetric rotation of alternate (001) triangular faces of $A^{F}O_6$ metaprism columns, which are corner-connected to BO_4 tetrahedra, to accommodate changes in the size or stoichiometry of the channel contents (Mercier et al., 2006; White et al., 2005). The metaprism twist angle (φ) is sensitive to the relative dimensions of the framework and tunnel constituents and when $\varphi < 25^{o}$ the apatite is hexagonal. However, for larger φ unsatisfactory bond valence sums (BVS) are resolved through $[100]_{hex}$ BO_4 rotations that reduce the symmetry to triclinic $P\bar{1}$ (Baikie *et al.*, 2007).

Two classes of monoclinic apatites appear either as a response to *X* anion sub-lattice misfits ($P2_1/b$), or in chemically complex compounds, from the need to introduce multiple crystallographic sites that accept cations of disparate size and charge ($P2_1/m$ and $P2_1$). For example, OH-*Ap* (Hughes *et al.*, 1989; Elliot *et al.*, 1973) and Cl-*Ap* (Kim *et al.*, 2000; Ikoma *et al.*, 1999) are reportedly dimorphic, adopting both hexagonal $P6_3/m$ and monoclinic $P112_1/b$ structures, although small compositional departures from $Ca_{10}(PO_4)_6(OH)_2$ and $Ca_{10}(PO_4)_6Cl_2$

may be a pre-requisite for the stabilization of those monoclinic forms. Nonetheless, it is clear that anti-parallel <001> offsets of the OH/Cl atoms along the tunnels are essential to avoid over-bonding (Le Page and Rodgers, 2005) and these displacements destroy the mirror symmetry in $P6_3/m$ and lead to a doubling along one a_{hex} axis.

Compositionally intricate natural apatites show a wide range of coupled ionic substitutions combined with varying degrees of non-stoichiometry (Pan and Fleet, 2002), that are facilitated through the crystallization of lower-symmetry analogues conforming to maximal non-isomorphic space groups of $P6_3/m$ (White and Dong, 2003). A typical representative is ellestadite (*El-Ap*), where the $2P^{5+} \leftrightarrow Si^{4+} + S^{6+}$ substitution leads to a monoclinic $P2_1$ structure idealized as $[Ca_4][Ca_6][(PO_4)_{1-2x}(SiO_4)_x(SO_4)_x]_6(F,Cl,OH)_2$ (Organova et al., 1994). Beyond chemically-induced symmetry modification, complex apatite nanostructures have been observed in synthetic materials that depart from thermodynamic equilibrium such as $[Ca,Pb]_{10}([V,P]O_4)_6(F,O)_{2-x}$ (Dong and White, 2004a; 2004b), or in equilibrated minerals, where it has been proposed that spinodal decomposition and phase separation take place (Ferraris et al., 2005).

In an earlier study, it was shown by conventional powder X-ray diffraction and transmission electron microscopy that gem-grade apatite from Brazil (Fig. 2) consists of host F-*Ap* (~450 nm domains) surrounding guest OH/Cl-*Ap* domains (~250 nm) that, in turn, encapsulate faceted nano-sized hydroxylellestadite (OH-*El*) crystals. The F-*Ap* and OH/Cl-*Ap* were described as hexagonal $P6_3/m$ while OH-*El* was assigned as monoclinic $P2_1/m$ symmetry (Ferraris et al., 2005) (Fig. 3). However, as symmetry reduction arising from light elements (especially the tunnel anions) could not be addressed, and some phase domains were electron-beam sensitive, supplementary single-crystal X-ray and neutron diffraction experiments,

combined with synchrotron powder X-ray diffraction are reported here to verify and extend the conclusions drawn from the previous work.

The examination of multiphase 'single' crystals by either X-ray or neutron diffraction is rarely attempted, in part because such materials would normally be considered inferior specimens. However, such analyses are feasible, as in the case of the co-determination of the structures of zirconolite and zirkelite crystals that were too small to separate into phase-pure grains (Mazzi and Munno, 1983). The current study, while being more ambitious with four apatites considered simultaneously is possible because the chemically distinct regions are texturally coherent, or almost so. In addition, the space-group relationships between apatites are well understood.

Experimental Methods

Electron Data Collection

In Ferraris *et al.* (2005) the composition of the apatite collected from Ipirá, Bahia Province, Brazil, was determined by electron microprobe analysis (EPMA) to be $(Ca_{3.95}Na_{0.05})Ca_{5.99}(P_{5.69}Si_{0.18}S_{0.13})O_{24}(F_{1.52}Cl_{0.12}OH_{0.36})$. The EPMA of apatite is analytically challenging (McCubbin et al., 2010; Pyle et al., 2002; Stormer et al., 1993) and the chemical composition determined in the previous study was obtained without any constraint to the overall charged balancing. Specifically, because EPMA cannot be used to determine OH, the 0.36 structural formula units (sfu) of hydroxyl were derived on the assumption that the channel ions sum to 2 per unit cell i.e. F + Cl + OH = 2. McCubbin *et al.* (2010) determined that a missing

structural component in the monovalent channel ion site of apatite must be greater than 0.16 sfu before it is above the minimum threshold for detection. The missing component of 0.36 sfu found in Ferraris et al. (2005) exceeds this minimum threshold for detection. In addition to the expected channel species found, Pan and Fleet (2002) noted that the apatite X-site can hold and number of anions including CO_3^{2-}, Br^-, I^-, S^{2-}, O^{2-} as well structural vacancies and electroneutral molecules such as H_2O; however, these were not detected in the previous study. Transmission electron microscopy (TEM) investigations were carried out on ion-milled crystallographically oriented slices. Sample and technical details for the TEM and EPMA are available in Ferraris *et al.* (2005).

Synchrotron Powder X-ray Diffraction (SPXRD)

Synchrotron powder X-ray diffraction data were collected using the X-ray Development and Demonstration Beamline of the Singapore Synchrotron Light Source that operates a Helios 2 storage ring at 700 MeV with a typical stored beam current of 300 mA. X-ray energy was selected with a Si (111) channel-cut monochromator blocked to be 1mm high vertically and focused to a horizontal width of 3.5 mm by the collimating mirror and slit system. The configuration yielded an X-ray beam of 0.01° divergence at 8.048 keV. The detector slit was adjusted to be 1mm high. The diffractometer was the Huber 4-circle system 90000-0216/0, with high-precision 0.0001° step size for the omega and two-theta circles using Bragg-Brentano geometry. The distance from entrance slit to sample was 688 mm and from sample center to detector 680 mm. The sample was gently pressed into a flat-plate sample holder in an attempt to reduce preferred orientation. In order to maximize the incident and diffracted X-ray intensities

most of the beam path was encapsulated in a plastic tube filled with helium gas. However, the sample itself was exposed to air. The data were collected using a step size of 0.02° with a counting time of 5 seconds per data point, which defined the FWHM of each reflection by at least 5 data points. All samples were scanned over the range 15°-140° in two-theta. Prior to analysis the raw data were normalized to the counts recorded by the incident-beam monitor. The data were analyzed using *TOPAS V4.1* (Bruker, 2008).

Single-Crystal Neutron Data Collection

Neutron diffraction data were gathered from a euhedral blue crystal (Fig. 2) on the Very Intense Vertical Alignment Laue Diffractometer (VIVALDI) at the Institut Laue-Langevin (ILL), Grenoble, France. VIVALDI uses Laue diffraction on a polychromatic thermal-neutron beam coupled with a large solid-angle (8 steradians) cylindrical image-plate detector, to increase the detection efficiency of the sum of diffracted intensities by one to two orders of magnitude compared with a conventional monochromatic experiment (McIntyre et al., 2006; Wilkinson et al., 2002). The apatite crystal of approximate dimensions 6 mm × 5 mm × 4 mm was wrapped in aluminium foil smeared with silicone grease and glued to a vanadium pin, then mounted in a helium-flow cryostat and cooled to 130 K. Five Laue diffraction patterns were collected at 20° intervals around the vertical axis perpendicular to the incident neutron beam, with each exposure lasting just 5 minutes (Fig. 4). The sample volume is considerably larger than the 1 mm^3, which is typical for structural studies on VIVALDI, but a further goal of this neutron study was to demonstrate that a sensible structural refinement could be obtained from such a large sample.

The large volume dictated in turn very short exposure times to avoid individual pixel counts in the recorded Laue patterns exceeding the maximum possible of 65535.

The diffraction patterns were indexed using the program LAUEGEN (Campbell, 1995; Campbell et al., 1998) and the reflections integrated using a 2D version of the σ(I)/I algorithm described by Wilkinson *et al.* (1988) and Prince *et al.* (1997). No absorption correction was necessary (μ = 0.038 cm^{-1}). The short exposure time necessitated a correction for the decay of 2.5% of the latent image during the 3.5 min readout. Correction was also made for the higher probability of neutron capture away from the equatorial plane by the ^{158}Gd found in natural abundance in the Gd_2O_3 scintillator of the image plate (R. O. Piltz, pers. commun.). The reflections were then normalized to a common incident wavelength, using a curve derived by comparing equivalent reflections and multiple observations, via the program LAUENORM (Campbell et al., 1986). Only reflections with wavelengths between 1.0 Å and 2.9 Å were accepted for the normalization procedure, as those outside this range were too weak, or had too few equivalents to allow determination of the normalization curve confidently. The total number of observed reflections accepted was 2426, which were averaged to give 414 unique reflections (R_{int} = 0.0046), of which 384 have $F^2 > 3\sigma(F^2)$. The resulting intensities were used in a full-matrix least-squares refinement using UPALS (Lundgren, 1982). An isotropic type I extinction correction was applied (Becker and Coppens, 1974). In the final refinement, the scale factor and the positional and anisotropic atomic displacement parameters for all atoms were refined, except for F, Cl and OH that were treated isotropically to give a total of 42 variables. The value of the goodness-of-fit is close to 1.0, indicating that a lower *R* factor cannot be expected. A summary of the crystal, data-collection and refinement parameters is given in Table 1. The neutron

scattering lengths of 0.4700, 0.5130, 0.5803, 0.5654, -3.7390 and 0.9577 were used for Ca, P, O, F, H and Cl respectively (Sears, 1993).

Single-Crystal X-ray Data Collection

A small fragment (0.1 mm × 0.1 mm × 0.1 mm) was cleaved from the large crystal used in the neutron diffraction study. Data were collected on a Bruker Smart Apex II three-circle diffractometer at 100 K using Mo *K*α radiation with a graphite monochromator over the angular range 2.5 to 30.5 2θ. A total of 542 reflections with $I>3\sigma(I)$ were collected and the structures refined using Jana 2006 (Petříček et al., 2006) utilizing the Superflip (Palatinus and Chapuis, 2007) structure-solution algorithm.

Analysis Strategy

In a review of reliable chemical end-member crystal-structure determinations, White and Dong (2003) found that approximately 60% of apatites conform to $P6_3/m$ (space group no. 176), with the remainder adopting, in decreasing order of abundance, $P6_3$ (173), *P*-6 (174), *P*-3 (147), $P2_1/m$ (11) or $P2_1$ (4) symmetry. Several space groups have been reported for F-*Ap*, Cl-*Ap*, OH-*Ap* and OH-*El*, with the first three most commonly described as $P6_3/m$. While this assignment is acceptable for F-*Ap* as noted before, OH/Cl cannot be located on the mirror plane as this is incompatible with bonding requirements. Therefore, in these latter cases, $P6_3/m$ is an average structure that reflects the disorder of the tunnel anion with the OH/Cl displaced off the mirror

plane along <001> with equal frequency (Leroy and Bres, 2001). Ellestadite is most reliably regarded as monoclinic $P2_1$ with a lattice metric close to hexagonal.

Results

Neutron Diffraction Data

Cell Parameter Refinement

Only the ratios of the linear lattice parameters can be obtained from the white-beam Laue technique. Our data gave a *c/a* ratio of 0.730, which is very close to that obtained from powder X-ray diffraction data for the *host-Ap*: $a = b = 9.4124(1)$ Å, $c = 6.8853(1)$ Å, $c/a = 0.7315$. (Table 1, Ferraris et al. (2005). There was no evident splitting or broadening of the Laue spots due to the slightly different *c*/*a* ratios of the coexisting apatite phases.

Space Group Selection

Several space groups were tested ($P6_3/m$, $P6_3$, $P2_1/m$, $P2_1$) with $P6_3/m$ proving superior and the statistics indicating an almost perfectly non-centric symmetry due to displacement of the asymmetric hydroxyl groups and chlorine atoms. Refinements using a monoclinic cell ($P2_1$) yielded slightly better *R*-values as compared to $P6_3/m$; however, the difference was insignificant, especially when the extra number of parameters was considered (~200 versus 42).

Composition

According to the electron microprobe (EPMA) and selected area electron diffraction (SAED) study of Ferraris *et al*. (2005) the host F-*Ap* accounts for ~76 wt% and the guest Cl-*Ap*, OH-*Ap* and OH-*El* ~6, ~13 and ~5 wt% respectively. The F position of fluorapatite is usually listed as 2*a* (0, 0, ¼), and a preliminary refinement of the occupancy factor of this F site gave 0.76(1) when refining isotropically, but 0.94(1) when refining anisotropically, with elongation along the *c*-axis. The 0.76 F perfectly agrees with the value obtained by EPMA. Alternatively, the 0.94 would be consistent with 0.76 F + 0.18 O, where the oxygen is associated with H as OH groups, keeping in mind that the scattering lengths of F and O are almost equal (0.5654 and 0.5803 × 10^{-12} cm respectively). This interpretation would also be reasonable from a crystal chemical point of view: the 2*a* site which is surrounded by a triangle of A^T cations results in over-bonding for O which is marginally displaced along [001]. Therefore, refinement included release of the O (4e; 0 0 *z*) to yield a *z* coordinate of 0.316(12). This places the hydroxyl H atom at $z \sim 0.47$, assuming an O-H bond length of ≈ 1 Å. Difference Fourier mapping confirmed the hydroxyl O near $z = 0.32$ and located the hydroxyl H around $z = 0.5$. The hydrogen can be refined at a position close to this location.

Refinements of the X-ray data showed that no crystalline Cl-*Ap* was present (Ferraris et al., 2005), even though its cell parameters are sufficiently different to permit ready detection. This suggests that chlorine atoms, which are too large to displace F, are for the most part distributed randomly throughout the crystal, although chlorine-rich domains (~250 nm) can be located by analytical TEM. Neither did extensive difference Fourier mapping show excess scattering density attributable to Cl, which would normally appear at $z = 0.4432$ (Mackie and

Young, 1974). However, this location places Cl very close to the H atom, as observed in the averaged, overall structure. It was therefore unsurprising that a refinement for Cl restrained around z = 0.4432 failed to reveal a scattering center. A Cl positioned at (0, 0, 0) (Hendricks et al., 1932), or the equivalent (0, 0, 0.5), were similarly discounted. McCubbin *et al*. (2008) showed via $^{19}F(^{35}Cl)$ TRAPDOR NMR that low OF F-Cl apatite has F and Cl mixed in the apatite channel such that all Cl ions have neighboring F atoms, and with the Cl ions positioned at z = 0.126. However, no scattering center was observed at this site in the current work, which is probably related to the low Cl concentrations present in the samples studied.

While Ca is distributed over the A^F and A^T sites, the Na is expected to partition almost exclusively into the A^F framework position, as alkali ions (Na through Cs) become significantly over-bonded in the A^T site. A reconnaissance refinement that placed only Ca at the *A* sites was consistent with a small amount of Na entering the A^F. Assuming that the A^F and A^T sites are fully occupied, the scattering length for each was adjusted to give an occupancy of 1, leading to about $Na_{0.09}$ at A^F, a result not significantly different from the $Na_{0.05}$ obtained by chemical analysis. The same procedure indicated pure speciation at A^T (Ca) and O1, O2 and O3 using the standard scattering lengths (Sears, 1993). A refinement of the occupancy factor of P indicates the presence of 3 wt% OH-*El*, assuming equimolar amounts of Si and S. This result is slightly less than the 5 wt% found by Ferraris *et al.* (2005). The final refined atomic positions and bond lengths are given in Tables 2 and 3 and the final refined structure is shown in Figure 5.

Single Crystal X-ray Diffraction

The refinement of single-crystal X-ray diffraction data gave essentially the same results as the neutron diffraction study but with an apparent improvement on the precision of the atomic positions and bond lengths (Tables 3 and 4). When only F was placed in the channel, the refinement gave this site as approximately 92 % occupied with a large anisotropic atomic displacement parameter (ADP) along the channel ($U_{33} \approx 0.06$). Using a similar protocol to the neutron refinement an oxygen atom was placed at a 4*e* Wyckoff position 0, 0, *z* ($z \approx 0.32$), with the ADP values for F and O refined isotropically and with their overall occupancy summed to unity. There was little difference in the reliability indices between a refinement including an F position with anisotropic displacement parameters or split positions with O and F. This is unsurprising as X-rays are interacting with a diffuse electron cloud rather than the point scattering achieved with neutrons. Similar to the neutron diffraction study, extensive Fourier mapping was carried out and a weak (≈ 0.5e) and diffuse scattering volume was found close to 0, 0, 0. Both H and Cl atoms were separately included into the refinement and yielded relative occupancies of ≈0.6 H or 0.02 Cl (with the isotropic ADP fixed at $U_{iso} = 0.02$). The additions of H or Cl to the apatite channel offered a slight improvement to the refinement indices but as X-rays are generally insensitive to hydrogen, the small differences may be considered insignificant. The occupancy of the A^F site refined as slightly less than unity (98% occupancy), confirming a limited incorporation of Na at this site.

Synchrotron Powder X-ray Diffraction (SPXRD)

The previous conventional powder X-ray diffraction study of the Brazilian apatite (Ferraris et al., 2005) noted that the *hk*0 reflections were broader than the 00*l* reflections suggesting the presence

of separate apatite phases. However, the resolution of the experiment was insufficient for the separation of anisotropic reflections into individual phases. Therefore data were collected on the same sample using monochromatic synchrotron radiation.

Preferred orientation was observed because a relatively coarse, manually ground powder was used. As a consequence, only a finite number of diffracting crystallites were illuminated by the beam resulting in a non-random distribution of orientations. To avoid textured effects, a micronizing mill (McCrone, UK) was employed; however this procedure also removed reflection anisotropy/splitting, suggesting the micronization was modifying the sample composition. This is not unexpected as recent work has shown that lanthanum silicate apatite electrolytes can be synthesized at room temperature by mechanically milling the constituent oxides La_2O_3 and SiO_2 (Fuentes et al., 2006). However, the objective of this experiment was to determine whether distinct apatite phases could be identified, therefore a Pawley fit of the data was performed to extract their lattice parameters. A three-phase fit containing two hexagonal phases and a monoclinic ellestadite-type phase, as identified by electron microscopy is shown in Figure 6 and clearly validates anisotropic reflection broadening and peak splitting. A Pawley fit containing three hexagonal phases was also attempted; however, the reliability indices and profile fit indicated the former was the preferred choice. The R_{wp} from the three-phase fitting (21.0%) offered a significant improvement to a two-phase fit (28.9%), and the considerably higher single phase fit (35.8%). The lattice parameters for the two hexagonal apatite phases are in good agreement with those expected for F-*Ap* [a = 9.4246(4), c = 6.8816(2) Å] and OH-*Ap* [a = 9.4118(2), c = 6.8855(3) Å], and these, together with the refined lattice parameters of ellestadite-type phase [a = 9.4122(3), b = 9.3999(1), c = 6.8940(2) Å, γ = 119.877(3)°, in space group $P112_1/m$] are comparable to values determined from electron diffraction (Ferraris et al.,

2005). In addition, the refined data agree with earlier electron microscopy and conventional powder X-ray diffraction experiments that noted there was a greater variation in the *a* parameter as a function of composition.

Discussion

This refinement of the individual components of a multi-domain single crystal is essentially complementary to the data obtained by electron microscopy with the single-crystal experiments providing an average model of the crystal chemistry, with the powder experiment revealing phase separation into chemically distinct domains. Agreement between the techniques provides a high level of confidence that the description of this Brazilian apatite is essentially complete. Analysis of the single-crystal XRD and neutron diffraction patterns was possible because all the apatite domains, F-*Ap*, OH-*Ap*, Cl-*Ap* and OH-*El*, were topotaxic, and within the resolution of the experimental techniques, the diffracted intensity of individual reflections was the sum of contributions from each phase. Nonetheless, small differences in cell parameters (9.39 Å < *a* < 9.43 Å and 6.88 Å < *c* < 6.90 Å) are present, as shown by synchrotron powder X-ray diffraction experiments. High-resolution electron microscope images found that local strain preserves the coherency of adjacent domains (Ferraris *et al*., 2005). However, the mismatch is minimal as the Laue images give no indication of diffuse scattering. While the location of F at 2*a* (0 0 ¼) within the A^T triangle is consistent with earlier studies (Sundarsanan *et al*., 1972), Cl is usually reported at 4*e* (0 0 *z*), with *z* in the range of 0.3-0.4 (Mackie et al., 1972). The bond valence sum (BVS) for Cl at (0, 0, 0.25) is 3.4, and evidently unsatisfactory, while a somewhat better location at *z* = (0, 0, 0.4432), gives a BVS of 1.71. The best value of

1.47 was obtained with Cl at (0, 0, 0.5), but this remains unacceptably large and shows the lattice is F dominant. In the reported Cl-*Ap* structure the BVS is 1.05, very close to the expected value of 1. In this structure, the Cl…Ca distance is slightly larger than found in F-*Ap* and OH-*Ap*. The partitioning of Na^{+} to the A^{F} site and equimolar substitutions of Si^{4+} + S^{6+} to the *B*-site are explicable in terms of ionic size and charge. The BVS for the refined proportions of P + Si + S in BO_4 is 4.90, close to the expected value of 5 (Table 4). The BVS for Ca in $A^{F}O_4$ is 1.72 and slightly lower than the formal valence due to the minor substitution of Ca by Na, while $A^{T}O_6X$ yields 2.01 that is consistent with full occupancy by Ca. An outstanding matter is the question of the true symmetry of the ellestadite component. While natural ellestadite is apparently monoclinic, a recent investigation of synthetic $Ca_{10-y}(SiO_4)_3(SO_4)_3Cl_{2-x-2y}F_x$ found $P6_3/m$ as the best crystallographic model across the series (Fang et al., 2011). At present, the data concerning this mineral is rather limited and further work is needed to establish the extent of Si^{4+}/S^{6+} and Na^{+} substitution for P^{5+} and Ca^{2+}, respectively, required to promote lattice distortion.

It can be concluded that the Brazilian apatite contains four phase types. The tunnel anions F are at fixed special positions along <001>, while the anions Cl and OH are displaced in a disordered fashion, with the suggestion that O-H···O-H··· hydrogen-bonded chains form in localized regions, such that balanced antisymmetric ordering avoids poling. The $A^{F}O_6$ metaprism twist angle of 23.4° for the average structure is consistent with previously reported values for the end members (F-*Ap* = 23.3°; OH-*Ap* = 23.2°; Cl-*Ap* = 19.1°) and confirms that the chlorine component is relatively insignificant.

From the geological and petrological view point, the nanostructure of the Ipirà apatite "single" crystals possibly arises from consecutive, or nested, spinodal decompositions. The amplitudes of the compositional modulations are assumed constant, with long wavelength (about

400-500 nm) separation of host F-Ap, and guest OH-Ap and Cl-Ap arising from the bulk composition. Before, during or after this long wave event, decomposition of higher frequency (about 10 nm) lead to the formation of OH-El. This combination of periodicities suggests that the Ipirà apatite experienced at least two significant geothermometric events.

A first long period modulation would have developed close to the coherent spinodal decomposition temperature resulting in the separation of X anions primarily and the formation of fluorine-rich and chlorine rich apatites. This kinetically-driven phase separation is interpreted to coincide with the geological age (El-Rey Silva et al. 1996) of the host rocks. The higher frequency modulation possibly occurred as a result of a short time episode at slightly higher temperatures (contact metamorphism) during late intrusion of basic bodies (El-Rey Silva et al., 1996), was diffusion-dependent, and resulted in the formation of smaller ellestadite domains. If this later event was above the coherent spinodal decomposition temperature, exsolution of OH-El by homogeneous nucleation may be the preferred mechanism.

The unexpected co-existence of multiple phases in this apatite gem stone illustrates the complexity of this intriguing structural family and the need to examine these materials using probes of complementary sensitivity and resolution. It seems probable that natural and synthetic apatites may exhibit composite microstructures and lower symmetry than presently recognized. Such features may prove important when optimizing the functionality of apatites designed as heterogeneous catalysts and solid electrolytes. This study has also demonstrated that highly credible structural data can be obtained very rapidly by modern neutron Laue diffraction from large single crystals, to give a bulk averaging over the phases in a non-destructive manner.

Acknowledgements

This work was supported by MOE Tier 2 and A*Star PSF grant numbers T208B1212 and 082 101 0021 respectively. Crystals were generously provided by our Brazilian colleague Dr. R. Wegner (Departamento de Mineração e Geologia, Campus II UFPb, CP 10094 58.109-970, Campina Grande Pb, Brazil).

Table 1. Crystallographic data and refinement parameters from the single crystal X-ray and neutron diffraction data.

Formula	$A_{10}B_6O_{24}F_{1.428}(OH)_{0.696}$*	$A_{10}B_6O_{24}F_{1.46}O_{0.54}$
	Neutron	X-ray
T (K)	130	100
Wavelength (Å)	$1.0 \leq \lambda \leq 2.9$	0.71073
Crystal system	Hexagonal	Hexagonal
Space Group	$P6_3/m$	$P6_3/m$
Unit cell dimensions		
a (Å)	9.3687**	9.3687(2)
c (Å)	6.8739**	6.8739(1)
V (Å^3)	522.51(1)	522.51(1)
Z	2	2
D_c (g.cm^{-3})	3.176	3.2044
μ, cm^{-1}	0.038	3.106
Reflections collected	2426	8078
Independent Reflections. (R_{int})	414 (0.0046)	551
Data/restraints/parameters	408/0/42	542/0/41
R indices (all data)		
R (F^2)	0.0554	0.0198
wR (F^2)	0.0605	0.0642
GoF (F^2)	1.128	1.56
R indices ($I > 3\sigma(I)$)		
R (F^2)	0.0515	0.0200
wR (F^2)	0.0599	0.0643
GoF (F^2)	1.163	1.58

* A = Ca + Na; B = P + Si +S

** The absolute scale of the unit-cell lengths cannot be determined in the white beam Laue method; c was fixed at the X-ray value

Table 2. Fractional coordinates and displacement parameters derived from single crystal neutron diffraction data collected at 130K.

Fractional Coordinates

	Wyckoff	*x*	*y*	*z*	Occ.	U_{eq}
A^{F*}	4*f*	1/3	2/3	-0.0013(5)	0.95	0.0084(13)
A^{T}	6*h*	0.2438(2)	-0.0065(2)	1/4	1	0.0018(11)
B^{**}	6*h*	0.3986(2)	0.3690(2)	1/4	1	0.0074(9)
O(1)	6*h*	0.3267(2)	0.4838(2)	1/4	1	0.0084(8)
O(2)	6*h*	0.5880(2)	0.4662(2)	1/4	1	0.0107(8)
O(3)	12*i*	0.3417(2)	0.2565(2)	0.0702(3)	1	0.0135(7)
F	2*a*	0	0	1/4	0.714(5)	0.0051(12)
O(4)	4*e*	0	0	0.316(12)	0.174(9)	0.0051
H	4*e*	0	0	0.472(6)	0.174	0.0061(15)

Displacement Parameters

	U_{11}	U_{22}	U_{33}	U_{12}	U_{13}	U_{23}
A^{F}	0.0075(9)	0.0075	0.0102(35)	0.0037(5)	0	0
A^{T}	0.0041(10)	0.0010(10)	0.0020(31)	0.0001(8)	0	0
B	0.0070(9)	0.0099(9)	0.0054(24)	0.0056(7)	0	0
O(1)	0.0122(8)	0.0087(8)	0.0044(20)	0.0068(7)	0	0
O(2)	0.0055(7)	0.0099(8)	0.0165(21)	0.0032(6)	0	0
O(3)	0.0187(7)	0.0106(6)	0.0112(19)	0.0099(5)	-0.0059(7)	-0.0025(7)

* *A* = Ca + Na
** *B* = P +Si + S

Table 3. Selected distances (Å) and bond valence sums for BO_4, A^FO_6 and A^TO_6 from single crystal neutron and X-ray diffraction data.

Bond	Distance (neutron)	Distance (XRD)
A^F- O(1) × 3	2.412(3)	2.3963(9)
A^F- O(2) × 3	2.436(3)	2.4466(13)
A^F- O(3) × 3	2.796(3)	2.7951(11)
A^T- O(1) × 1	2.687(3)	2.6813(17)
A^T- O(2) × 1	2.358(2)	2.3663(14)
A^T- O(3) × 4	2.343(2), 2.486(2)	2.3436(10), 2.4896(10)
A^T- F × 1	2.315(2)	2.3104(5)
A^T- O(4)	2.359 (20)	2.3409(4)
B – O(1) × 1	1.528(2)	1.5346(19)
B – O(2) × 1	1.540(3)	1.5372(14)

B – O(3) × 2	1.537(2)	1.5364(9)
O(4) – H	1.07(4)	-
BO_4	4.90(P^{5+} + Si^{4+} + S^{6+})	4.93
A^FO_6	1.72 (Ca^{2+} + Na^{+})	1.73
A^TO_6	2.01 (incl. 2 OH^-)	2.07

Table 4. (a) Fractional coordinates and (b) displacement parameters derived from single crystal X-ray diffraction data collected at 100K.

Fractional Coordinates

	Wyckoff	***x***	***y***	***z***	**Occ.**	U_{eq}
A^{F*}	4*f*	1/3	2/3	0.00111(5)	0.98	0.00776(16)
A^T	6*h*	0.24293(4)	-0.00716(4)	1/4	1	0.00724(18)
B^{**}	6*h*	0.39852(6)	0.36890(6)	1/4	1	0.0057(2)
O(1)	6*h*	0.32624(18)	0.48413(15)	1/4	1	0.0081(5)
O(2)	6*h*	0.58796(17)	0.46605(16)	1/4	1	0.0109(5)
O(3)	12*i*	0.34215(13)	0.25650(10)	0.07012(12)	1	0.0129(4)
F	2*a*	0	0	1/4	0.730(10)	0.0101(8)
O(4)	4e	0	0	0.305(3)	0.135(5)	0.0101(8)

Displacement Parameters

	U_{11}	U_{22}	U_{33}	U_{12}	U_{13}	U_{23}
A^F	0.0091(2)	0.0091(2)	0.0051(3)	0.00454(10)	0	0
A^T	0.0080(3)	0.0066(2)	0.0070(3)	0.00355(15)	0	0
B	0.0066(3)	0.0058(3)	0.0056(3)	0.00381(19)	0	0
O(1)	0.0099(7)	0.0072(6)	0.0092(6)	0.0057(5)	0	0
O(2)	0.0069(6)	0.0084(7)	0.0171(6)	0.0037(5)	0	0
O(3)	0.0216(5)	0.0110(5)	0.0094(4)	0.0106(4)	-0.0064(4)	-0.0035(3)

* *A* = Ca + Na

** *B* = P +Si + S

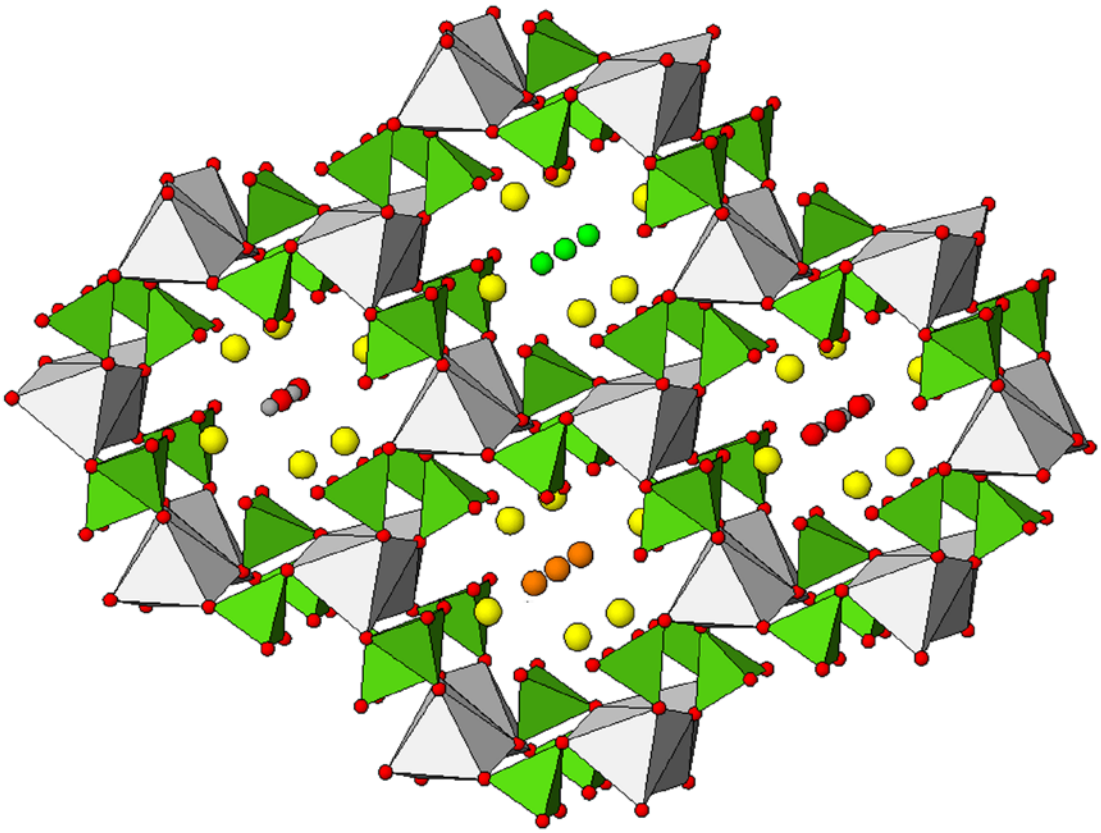

Figure 1. A schematic illustration of the framework motif and types of tunnel-anion order found in Brazilian apatite gems. The grey AO_6 polyhedra are metaprisms containing calcium and sodium, while the green BO_4 tetrahedra accommodate phosphorus, silicon and sulphur. The tunnels contain calcium (yellow) and the tunnel anions fluorine (green), chlorine (orange) and hydroxyl (oxygen red, hydrogen grey) in two orientations. (ATOMS, Dowty, 2002).

Figure 2. The apatite crystal used for the neutron diffraction experiment.

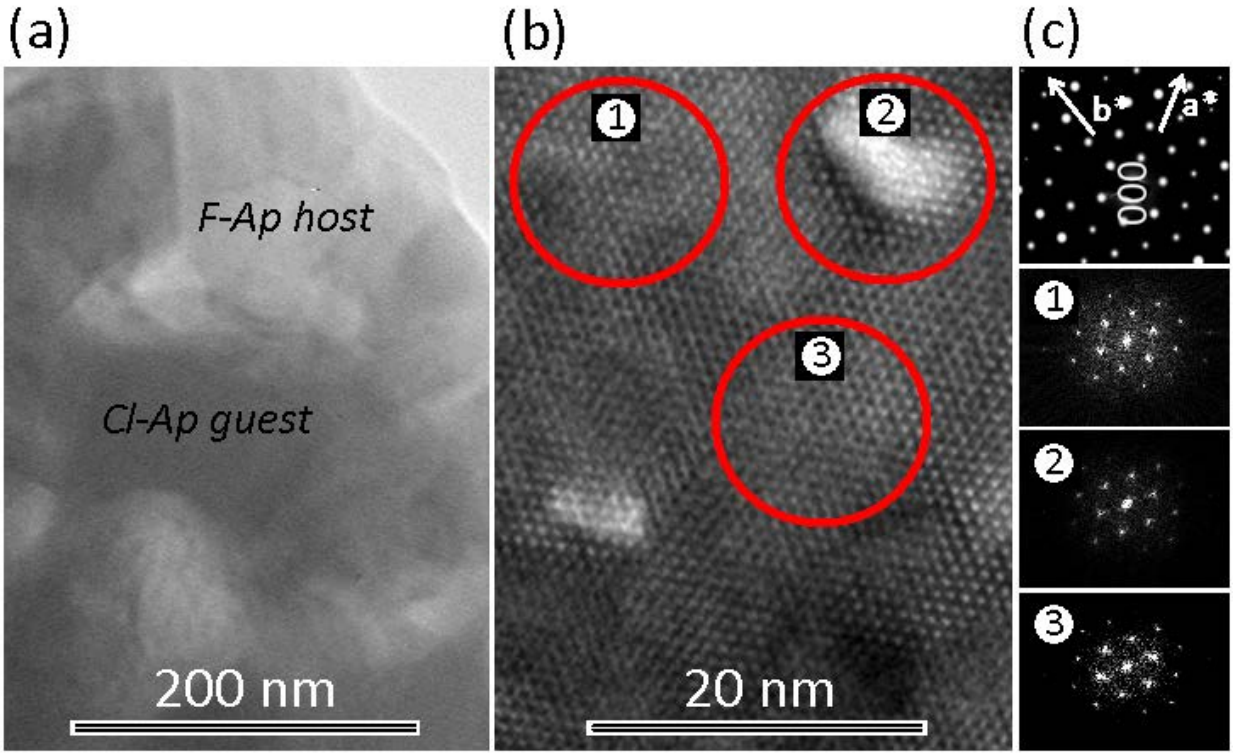

Figure 3. Transmission electron microscopy (a) a [001] bright field image containing the F-*Ap* host (lighter contrast) and Cl-*Ap* guest apatite (dark contrast); (b) the [001] high resolution image where ellestadite nanodomains, richer in Na+Si+S, are embedded in host and guest apatites. (c) Uppermost the pattern obtained from a crystal volume containing the region shown in (a) is given. FFT were collected from (1) an ellestadite region, (2) and electron-beam damaged region and (3) a guest region. Small changes on orientation are evident. Elsewhere, energy dispersive X-ray microanalysis has been used to confirm the compositional uniqueness of these regions (Ferraris et al., 2005).

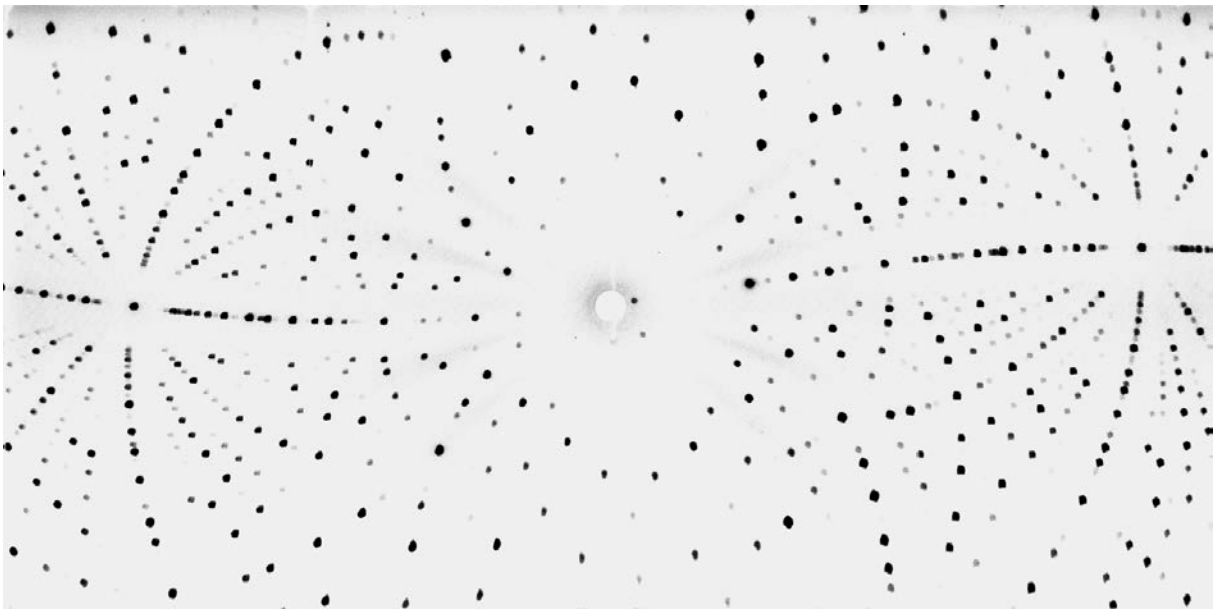

Figure 4. Laue diffraction pattern collected at VIVALDI, ILL.

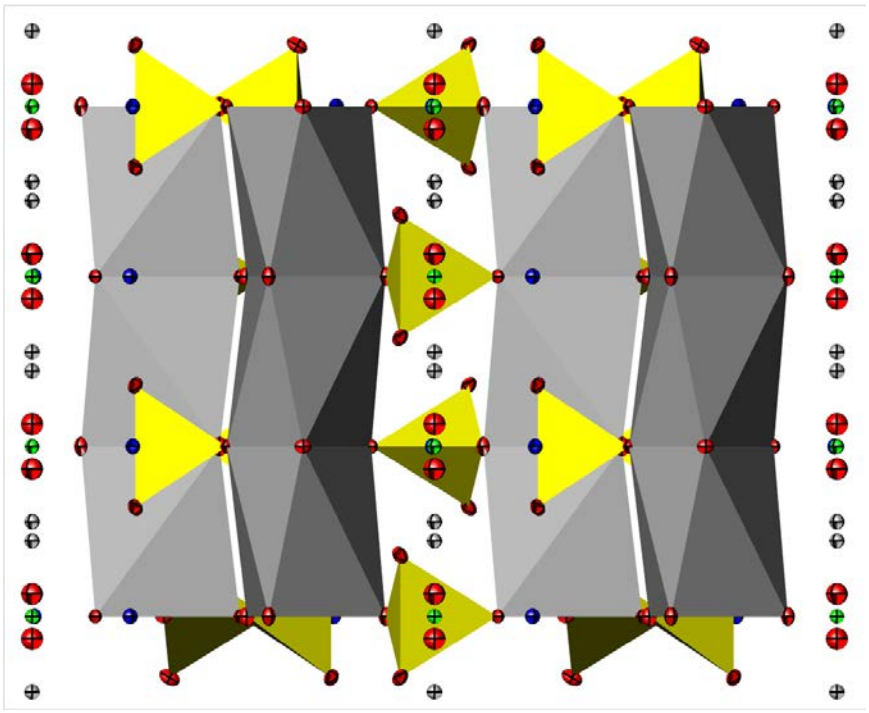

Figure 5. Structural representation of the single crystal neutron diffraction refinement. The red, green and grey ellipsoids represent the oxygen, fluorine and hydrogen atoms respectively.

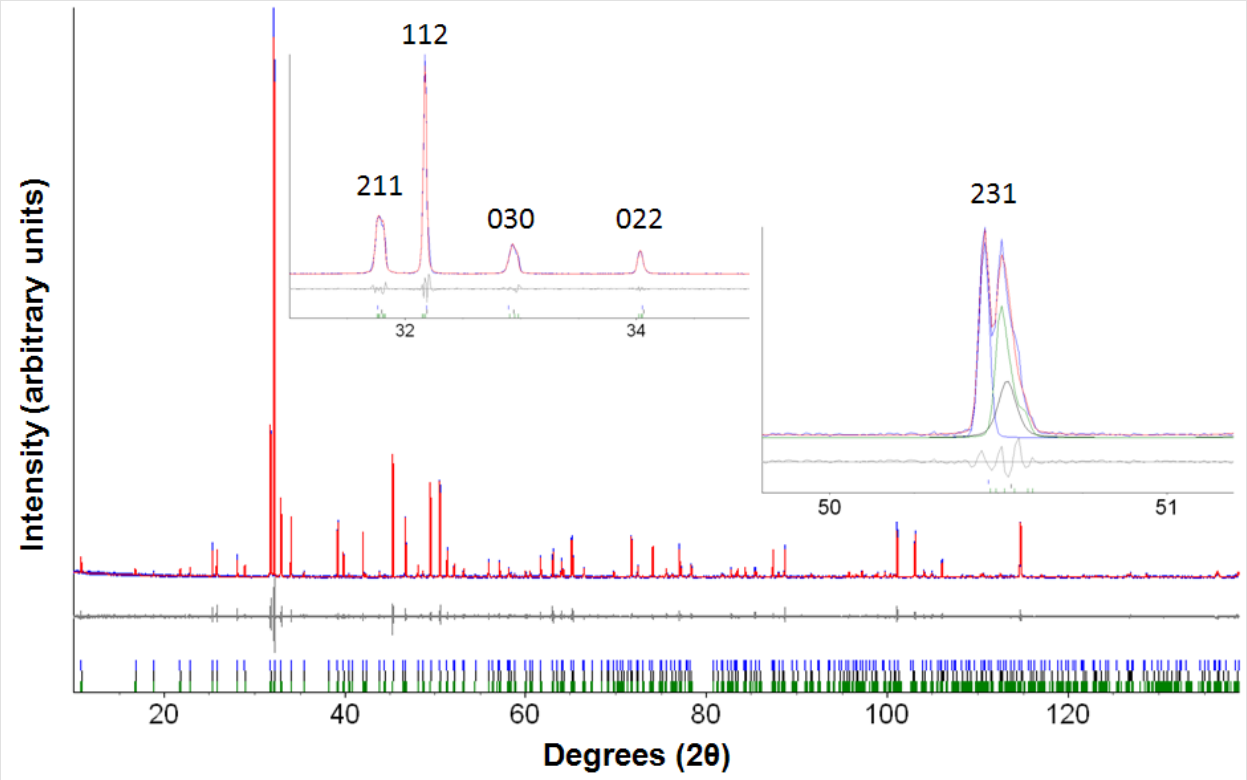

Figure 6. Pawley fit of the synchrotron data for the Brazilian apatite: (a) whole pattern; (b) selected region of the low angle data showing reflections broadening and partial splitting; (c) selected region of the high angle data showing a clear splitting of reflections and the requirement of three phases to fit the data.

References

Baikie, T., Mercier, P.H.J., Elcombe, M.M., Kim, J.Y., Page, Y.L., Mitchell, L.D., and White, T.J. (2007) Triclinic Apatites. Acta Crystallographica B, 63, 251-256.

Becker, P.J., and Coppens, P. (1974) Extinction within the Limit of Validity of the Darwin Transfer Equations. I. General Formalisms for Primary and Secondary Extinction and Their Application to Spherical Crystals. Acta. Crystallographica A, 30, 129-147.

Bruker. (2008) Topas Version 4.1. Bruker AXS Inc., Madison, Wisconsin, USA.

Campbell, J.W. (1995) LAUEGEN, an X-windows-based program for the processing of Laue X-ray diffraction data. Journal of Applied Crystallography, 28, 228-236.

Campbell, J.W., Habash, J., Helliwell, J.R., and Moffat, K. (1986) Information quarterly for Protein Crystallogr. No 18, SERC Daresbury Laboratory, Warrington, England, 23.

Campbell, J.W., Hao, Q., Harding, M.M., Nguti, N.D., and Wilkinson, C. (1998) Laugen version 6.0 and INTLDM. Journal of Applied Crystallography, 31, 496-502.

Dong, Z., and White, T.J. (2004a) Calcium-lead fluoro-vanadinite apatites. I Disequilibrium structures. Acta Crystallographica B, 60, 138-145.
-. (2004b) Calcium-lead fluoro-vanadinite apatites. II. Equilbrium structures. Acta Crystallographica B, 60, 146-154.
El-Rey Silva, L.J.H., Oliveira, J.G., and Gaal, E.G. (1996) Implication of the Caraiba deposits structural controls on the emplacement of the Cu-bearing hypersthenites of the Curaça valley, Bahia-Brazil. Revista Brasileira de Geociências., 26, 181-196.
Fang, Y., Ritter, C., and White, T. (2011) The crystal chemistry of $Ca_{10-y}(SiO_4)_3(SO_4)_3Cl_{2-x-2y}F_x$ ellestadite. Inorganic Chemistry, 50, 12641-12650.
Ferraris, C., White, T.J., Plevert, J., and Wegner, R. (2005) Nanometric modulation in apatite. Physical Chemistry of Minerals, 32, 485-492.
Fuentes, A.F., Rodríguez-Reyna, E., Martínez-González, L.G., Maczka, M., Hanuza, J., and Amador, U. (2006) Room-temperature synthesis of apatite-type lanthanum silicates by mechanically milling constitutent oxides. Solid State Ionics, 177, 1869-1873.
Hendricks, S.B., Jefferson, M.E., and Mosley, V.M. (1932) The crystal structures of some natural and synthetic apatite-like substances. Zeitschrift für Kristallographie, 81, 352-369.
Kay, M.I., Young, R.A., and Posner, A.S. (1964) Crystal structure of hydroxyapatite. Nature, 204, 1050-1052.
Le Page, Y., and Rodgers, J.R. (2005) Quantum software interfaced with crystal-structure databases: tools, results and perspectives. Journal of Applied Crystallography, 38, 697-705.
Leroy, N., and Bres, E. (2001) Structure and substitutions in fluorapatite. European Cells & Materials Journal, 2, 36-48.
Lundgren, J.O. (1982) Crystallographic Computer Programs, Report UUIC-B134-05, Institute of Chemistry, University of Uppsala, Sweden.
Mackie, P.E., Elliott, J.C., and Young, R.A. (1972) Monoclinic structure of synthetic $Ca_5(PO_4)_3Cl$, chloroapatite. Acta Crystallographica B, 28, 1840-1848.
Mackie, P.E., and Young, R.A. (1974) Fluorine-chlorine interaction in fluor-chlorapatite. Journal of Solid State Chemistry, 11(4), 319-329.
Mazzi, F., and Munno, R. (1983) Calciobetafite (new mineral of the pyrochlore group) and related minerals from Campi Flegrei, Italy: crystal structures of polymignyte and zirkelite: comparison with pyrochlore and zirconolite. American Mineralogist, 68, 262-276.
McCubbin, F.M., Mason, H.E., Park, H., Philips, B.L., Parise, J.B., Nekvasil, H., and Lindsley, D.H. (2008) Synthesis and characterization of low-OH-fluor-chlorapatite: A single crystal XRD and NMR spectroscopic study. American Mineralogist, 93, 210-216.
McCubbin, F.M., Steele, A., Nekvasil, H., Schneiders, A., Rose, T., Fries, M., Carpenter, P.K., and Jolliff, B.L. (2010) Detection of structurally bound hydroxyl from Apollo mare basalt 15058, 128 using TOF-SIMS. American Mineralogist, 95, 1141-1150.
McIntyre, G.J., Lemée-Cailleau, M.-H., and Wilkinson, C. (2006) High-speed neutron diffraction comes of age. Physica B, 385-386, 1055-1058.
Mercier, P.H.J., Page, Y.L., Whitfield, P.S., and Mitchell, L.D. (2006) Geometrical parameterization of the crystal chemistry of $P6_3/m$ apatite. II. Precision, accuracy and numerical stability of the crystal-chemistry Rietveld refinement. Journal of Applied Crystallography, 39, 369-375.

Organova, N.I., Rastsvetaeva, R.K., Kuz'mina, O.V., Arapova, G.A., Litsarev, M.A., and Fin'ko, V.I. (1994) The crystal structure of low-symmetry ellestadite in comparison with other apatite like structures. Kristallografiya, 39, 278-282.

Palatinus, L., and Chapuis, G. (2007) Superflip - a computer program for the solution of crystal structures by charge flipping in arbitrary dimensions. Journal of Applied Crystallography, 40, 786-790.

Pan, Y., and Fleet, M.E. (2002) Composition of the apatite-group minerals: substitution mechanism and controlling factors. Reviews in Mineralogy and Geochemistry, 13-49.

Petriček, V., Dusek, M., and Palatinus, L. (2006) Jana2006. The crystallographic computing system., Institute of Physics, Praha, Czech Republic.

Prince, E., Wilkinson, C., and McIntyre, G.J. (1997) Comparison of the σ(I)/I and Least-Squares Methods for Integration of Bragg Reflections. Journal of Applied Crystallography, 30, 133-137.

Pyle, J.M., Spear, F.S., and Wark, D.A. (2002) Electron microprobe analysis of REE in apatite, monazite and xenotime: Protocols and pitfalls. Phosphates: Geochemical, Geobiological, and Materials Importance, 48, 337-362.

Sears, V.F. (1993) International Tables for Crystallography. Academic Publishers, Dordrecht, Kluwer.

Stormer, J.C., Pierson, M.L., and Tacker, R.C. (1993) Variation of F-X-ray and Cl-X-ray intensity due to anisotropic diffusion in apatite during electron-microprobe analysis. American Mineralogist, 78, 641-648.

Sudarsanan, K., Mackie, P.E., and Young, R.A. (1972) Comparison of synthetic and mineral fluorapatite, $Ca_5(PO_4)_3F$, in crystallographic detail. Materials Research Bulletin, 7, 1331-1338.

White, T.J., and Dong, Z. (2003) Structural derivation and crystal chemistry of apatites. Acta Crystallographica B, 59, 1-16.

White, T.J., Ferraris, C., Kim, J., and Madhavi, S. (2005) Apatite - An adaptive framework structure. Reviews in Mineralogy and Geochemistry, 57, 307.

Wilkinson, C., Cowan, J.A., Myles, D.A.A., Cipriani, F., and McIntyre, G.J. (2002) VIVALDI - A Thermal-Neutron Laue Diffractometer for Physics, Chemistry and Materials Science. Neutron News, 13, 37-41.

Wilkinson, C., Khamis, H.W., Stansfield, R.F.D., and McIntyre, G.J. (1988) Integration of single-crystal reflections using area multidetectors. Journal of Applied Crystallography, 21, 471-478.